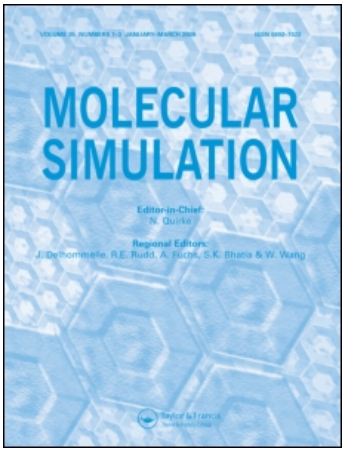

Molecular Simulation
Publication details, including instructions for authors and subscription information:
http://www.informaworld.com/smpp/title~content=t713644482

Sorption strains and their consequences for capillary condensation in nanoconfinement

Gerrit Günther[a]; Martin Schoen[a]
[a] Stranski-Laboratorium für Physikalische und Theoretische Chemie Sekr. C 7, Fakultät für Mathematik und Naturwissenschaften, Technische Universität Berlin, Berlin, Germany

First published on: 21 September 2010

To cite this Article Günther, Gerrit and Schoen, Martin(2009) 'Sorption strains and their consequences for capillary condensation in nanoconfinement', Molecular Simulation, 35: 1, 138 — 150, First published on: 21 September 2010 (iFirst)
To link to this Article: DOI: 10.1080/08927020802412370
URL: http://dx.doi.org/10.1080/08927020802412370

Molecular Simulation
Vol. 35, Nos. 1–2, January–February 2009, 138–150

Taylor & Francis
Taylor & Francis Group

Sorption strains and their consequences for capillary condensation in nanoconfinement

Gerrit Günther[1] and Martin Schoen*

Stranski-Laboratorium für Physikalische und Theoretische Chemie Sekr. C 7, Fakultät für Mathematik und Naturwissenschaften, Technische Universität Berlin, Berlin, Germany

(*Received 5 May 2008; final version received 15 August 2008*)

We employ Monte Carlo simulations in a semi-grand canonical ensemble to investigate the impact of pore deformation on capillary condensation in nanoconfined fluids. The fluid is composed of 'simple' spherically symmetric molecules of the Lennard-Jones type. These molecules are confined to a slit pore, where the pore walls consist of a single layer of atoms distributed according to the (100) plane of the face-centred cubic lattice. The atoms are bound to their equilibrium lattice sites by harmonic potentials such that they can depart to some extent from these sites on account of their thermal energy and the interaction with the fluid molecules. Under experimentally realistic conditions, our results show that, upon filling with fluid, the effective average pore size first increases, and then drops sharply at capillary condensation. The pore eventually expands again when the density of the confined liquid-like phase is further enhanced. Compared with the ideal case of perfectly rigid substrates, deformability of the pore causes capillary condensation to shift to higher bulk pressures; that is, the liquid-like phases are destabilised relative to the confined gas-like phases.

Keywords: sorption strain; capillary condensation; nanoconfined fluids; Monte Carlo simulation

PACS: 02.70.Uu; 64.70.fm; 64.75.Jk; 68.35.Rh

1. Introduction

If a fluid is exposed to an external field, its phase behaviour and material properties will depend on the specific characteristics of the field. In the context of confined fluids, the solid matrix of a mesoporous material has frequently been treated as such an external field representing the walls of tiny pores of nanometre dimensions [1–3]. When adsorbed into these pores, their small size (i.e. the strength of the external field) causes a markedly different phase behaviour, structure and material properties of the adsorbate. For example, if the fluid–substrate attraction is sufficiently strong, condensation of the adsorbate occurs under thermodynamic conditions such that a corresponding bulk fluid is still an undersaturated gas. This phenomenon known as 'capillary condensation' is in principle predicted by the celebrated Kelvin equation [4] and has received quite a bit of experimental interest [5–10]. However, these early studies were basically concerned with disordered porous media such as controlled pore glasses, where the pores vary in shape and form an interconnected network. In the meantime, it has become feasible to synthesise other mesoporous materials that differ from the ones studied in these earlier works, in that they consist of more regular arrays of individual, disconnected, more or less cylindrical pores [11–13]. These new materials enable studies of nanoconfined fluids under more controlled conditions.

The experimental advances have also spurred a wealth of theoretical investigations of confined fluids from which a detailed molecular picture of capillary condensation emerged [1–3]. One of the most intriguing theoretical findings in more recent times concerns the prediction of novel phases in fluids confined between complex chemically decorated or geometrically sculptured substrates [14,15]. Here, the confined fluids' structure is imposed by the substrates through a template effect. Thus, these new confined thermodynamic phases have obviously no counterpart in any bulk system, which makes them particularly fascinating.

However, regardless of the specific nature of the model system studied theoretically, the confining substrates are conventionally treated as an inhomogeneous, anisotropic, but otherwise static external field. From this perspective, characteristic features of a confined fluid come about by superimposing the external field onto the intermolecular interactions between fluid molecules. In other words, no matter what changes occur in a confined fluid's thermodynamic state or mechanical properties, the solid substrates do not 'respond' or adjust themselves to any of these changes.

However, quite some time ago, Diestler and Schoen [16] showed that the mechanical properties and the structure of a confined fluid may be altered if the confining substrates are coupled thermally to the fluid phase.

*Corresponding author. Email: martin.schoen@fluids.tu-berlin.de

ISSN 0892-7022 print/ISSN 1029-0435 online

DOI: 10.1080/08927020802412370
http://www.informaworld.com

The physical situation studied in [16] is relevant to experimental work by Namatsu et al. [17] in which the authors show that thin silica plates separated by a distance of less than 200 nm may deform during the drying process after having been rinsed by water. More recently, Kowalczyk et al. [18] and Ustinov and Do [19] considered sorption-induced deformation of porous matrices. In both works, the pores may deform homogeneously; that is, the width of the entire pore may change upon increasing sorption. However, these earlier papers [18,19] do not explore the relationship between capillary condensation and pore deformation.

Moreover, it was recently demonstrated experimentally that SBA-15 pores may be deformed upon capillary condensation. Using *in situ* synchrotron X-ray diffraction (SAXD) and parallel measurements of an adsorption isotherm, Zickler et al. [20] demonstrated that a discontinuous phase transition in a confined fluid may alter the lattice constant characterising the (regular) mesoporous matrix. In [20], the correlation between the associated sorption strains and capillary condensation is established by comparing the form, location and intensity of the Bragg peaks determined in the scattering experiments with the steep variation of the adsorption isotherm at capillary condensation.

Sorption strains of the sort reported in [20] have also been observed earlier experimentally [21–23] and are discussed in terms of either continuum elasticity [21] or phenomenological thermodynamics [22]. It is also well known from solid–solid phase transitions that elastic strains may cause a shift of the phase boundaries [24]. However, to date, a microscopic analysis of the relationship between sorption strains and phase transitions in nanoconfined fluids is still lacking.

In the present work, we therefore intend to employ Monte Carlo simulations to address the following questions in conjunction with capillary condensation in a nanopore with locally deformable pore walls (cf. [18,19]):

(1) How are sorption strains related to the thermodynamic state of the confined fluid?
(2) Do sorption strains have an impact on capillary condensation?
(3) What is the relationship between sorption strains and the structure of the confined fluid?

To address these points, we organised the manuscript as follows. In Section 2, we introduce our model system and describe its thermodynamic and statistical–physical analyses in Sections 3.1 and 3.2, respectively. A key quantity that we wish to compute is the grand potential density ω of the confined fluid. We obtain ω via thermodynamic perturbation theory as we explain in Section 3.3. In Section 4.1, we analyse the relationship between substrate deformation and capillary condensation, whereas Section 4.2 is devoted to associated structural changes in the confined fluid. This paper concludes with a summary of our main findings in Section 5.

2. Model system

2.1 The model fluid

In this work, we consider a pure fluid consisting of N spherically symmetric molecules interacting with each other in a pairwise additive fashion. The fluid–fluid configurational energy can then be cast as

$$U_{\mathrm{ff}}(\boldsymbol{R}) = \frac{1}{2}\sum_{i=1}^{N}\sum_{j=1\neq i}^{N} u(r_{ij}), \tag{2.1}$$

where $r_{ij} = |\boldsymbol{r}_i - \boldsymbol{r}_j|$ is the distance between molecules i and j located at r_i and r_j, respectively, $\boldsymbol{R} \equiv (\boldsymbol{r}_1, \boldsymbol{r}_2, \ldots, \boldsymbol{r}_N)$ represents the configuration of fluid molecules,

$$u(r) = \begin{cases} u_{\mathrm{sh}}(r), & r \leq r_c \\ 0, & r > r_c \end{cases} \tag{2.2}$$

and

$$u_{\mathrm{sh}}(r) = u_{\mathrm{LJ}}(r) - u_{\mathrm{LJ}}(r_c) + \left.\frac{\mathrm{d}u_{\mathrm{LJ}}(r)}{\mathrm{d}r}\right|_{r=r_c} (r - r_{\mathrm{c}}) \tag{2.3}$$

is a so-called shifted-force potential. Unlike the full Lennard-Jones (LJ) potential

$$u_{\mathrm{LJ}}(r) = 4\varepsilon\left[\left(\frac{\sigma}{r}\right)^{12} - \left(\frac{\sigma}{r}\right)^{6}\right], \tag{2.4}$$

$u_{\mathrm{sh}}(r)$ vanishes continuously together with its first derivative (i.e. the intermolecular force) at the radius r_{c} of a cut-off sphere centred on $\boldsymbol{r}_i$. Throughout this work, we use $r_{\mathrm{c}} = 3.5\sigma$. Because of its definition, $u_{\mathrm{sh}}(r)$ is explicitly short range (unlike $u_{\mathrm{LJ}}(r)$), which is advantageous in the grand canonical ensemble Monte Carlo (GCEMC) simulations on which this work is based [3,25]. In Equation (2.4), σ is the 'diameter' of a fluid molecule and ε determines the strength of intermolecular interactions in the usual manner.

2.2 Thermally coupled substrates

Fluid molecules are confined by two planar solid substrates (Figure 1). For reasons that will become clear in Section 3, we need to consider a reference system, in which fluid molecules are confined between two structureless planar substrates. In the system of ultimate interest, the walls are thermally coupled to the confined fluid such that the walls can respond to whatever change in the thermodynamic state of the confined fluid may occur. In this latter case, the substrates are atomically structured

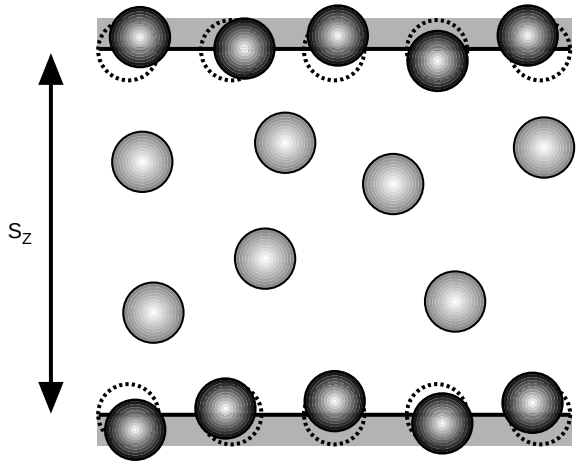

Figure 1. A two-dimensional schematic of the model system consisting of spherical fluid molecules (light grey) confined between two planar solid substrates separated by a distance s_z along the z-axis of the Cartesian coordinate system. In the reference system, the substrates are structureless as indicated by the black horizontal line and the area shaded in grey above and below this line. In the system of interest, the homogeneous substrates are replaced by discrete wall atoms (dark grey), where the equilibrium fcc (100) positions are represented by dashed circles.

and thermally corrugated as indicated by the sketch in Figure 1.

In both cases, there is a fluid–solid contribution to the total configurational energy. For the reference system, this contribution may be expressed as

$$U_{\mathrm{fs}}^{\mathrm{ref}} = \sum_{k=1}^{2} \sum_{i=1}^{N} \varphi^{[k]}(z_i), \tag{2.5}$$

where the fluid–solid interaction potential is given by

$$\varphi^{[k]}(z) = 2\pi\varepsilon\rho_{\mathrm{s}}\sigma^2 \left[\frac{2}{5} \left(\frac{\sigma}{z \pm s_z/2} \right)^{10} - \left(\frac{\sigma}{z \pm s_z/2} \right)^{4} \right]. \tag{2.6}$$

In Equation (2.6), $k = 1 \leftrightarrow +$ and $k = 2 \leftrightarrow -$, respectively, and we assume the solid substrates to be located at $z = \pm s_z/2$. Equation (2.6) is derived on the basis of the assumption that the substrate is composed of a single layer of solid atoms. These atoms are positioned according to the (100) structure of the face-centred cubic (fcc) lattice such that the nearest-neighbour distance between the atoms corresponds to the minimum of $u(r)$. This implies a lattice constant $\ell/\sigma = \sqrt[3]{4}$, such that the areal density $\rho\sigma^2 = 2^{-1/3}$. The solid atoms have been 'smeared' over the plane while the position of a fluid molecule is fixed at a point r_i [3]. Moreover, we take the parameters σ and ε to be the same for fluid molecules and wall atoms during the course of a simulation.

To realise walls that can respond to the confined fluid, we introduce our model of interest. Again, the substrates consist of individual solid atoms initially distributed according to the (100) plane of the fcc lattice at the areal density given above. The planes are initially in registry; that is, a specific atom in the upper substrate is exactly opposite its counterpart in the lower one and vice versa. This way the confined fluid can only be subjected to compressional strains (by changing, for example, s_z through external agents) but not to any shear deformation. Taking fluid molecules and substrate atoms to be identical (i.e. taking σ and ε to be the same for both species), we replace Equation (2.5) by

$$U_{\mathrm{fs}}(\boldsymbol{R}, \boldsymbol{R}_{\mathrm{s}}) = \zeta \sum_{k=1}^{2} \sum_{i=1}^{N} \sum_{j=1}^{N_{\mathrm{s}}} u\left(\left| \boldsymbol{r}_i - \boldsymbol{r}_j^{[k]} \right| \right), \tag{2.7}$$

where $N_{\mathrm{s}} = 2n^2$ is the total number of substrate atoms located in one wall and n is an integer specifying the number of unit cells of the fcc (100) plane. In Equation (2.7), $\boldsymbol{R}_{\mathrm{s}} = \left(\boldsymbol{r}_1^{[1]}, \ldots, \boldsymbol{r}_{N_{\mathrm{s}}}^{[1]}, \boldsymbol{r}_1^{[2]}, \ldots, \boldsymbol{r}_{N_{\mathrm{s}}}^{[2]} \right)$ represents the configuration of substrate atoms. The potential u in Equation (2.7) is given in Equation (2.2). The dimensionless parameter ζ in Equation (2.7) is introduced to vary the strength of the fluid–substrate interaction (see Equations (2.2)–(2.4), (2.7), and Section 4.2). If not stated otherwise, results in Section 4 are obtained for the case $\zeta = 1.0$ referring to equally strong fluid–fluid and fluid–substrate interactions. In any event, the distribution of the solid atoms and the rigidity of the substrates are such that fluid molecules cannot penetrate into the confining substrates as we have checked for all the simulations reported here.

In addition to U_{fs}, we include interactions between the substrate atoms themselves. The corresponding solid–solid energy is composed of two contributions and may be expressed as

$$U_{\mathrm{ss}} = \sum_{k=1}^{2} \left[\frac{1}{2} \sum_{i=1}^{N_{\mathrm{s}}} \sum_{j=1 \neq i}^{N_{\mathrm{s}}} u\left(\left| \boldsymbol{r}_i^{[k]} - \boldsymbol{r}_j^{[k]} \right| \right) + \kappa \sum_{i=1}^{N_{\mathrm{s}}} \left| \boldsymbol{r}_i^{[k]} - \boldsymbol{r}_{i0}^{[k]} \right|^2 \right], \tag{2.8}$$

where u is again given by Equation (2.2). On account of their interaction with both fluid molecules and other substrate atoms, each of the latter is free to depart from its equilibrium position ($\boldsymbol{r}_{i0}^{[k]}$) in the fcc (100) plane. In other words, substrate atoms are coupled thermally to the confined fluid and may move because of their kinetic energy. The first term on the right-hand side of Equation (2.8) is necessary because substrate atoms must not approach each other arbitrarily (and therefore unrealistically) close.

To prevent the substrates from 'melting', we bind each one of them to its equilibrium lattice site by introducing a harmonic potential (see the second term in brackets in Equation (2.8)), where $\kappa > 0$ determines the binding strength (i.e. the 'stiffness' of a harmonic spring). In other words, κ is a measure of rigidity of the substrates. Hence, in the system of interest, the total configurational energy may be expressed (see Equations (2.1), (2.7) and (2.8)) as

$$U\left(\boldsymbol{R},\boldsymbol{R}_{\mathrm{s}};\kappa\right) = U_{\mathrm{ff}}(\boldsymbol{R}) + U_{\mathrm{fs}}\left(\boldsymbol{R},\boldsymbol{R}_{\mathrm{s}}\right) + U_{\mathrm{ss}}(\boldsymbol{R}_{\mathrm{s}};\kappa) \quad (2.9)$$

and depends on $\boldsymbol{R}$, $\boldsymbol{R}_{\mathrm{s}}$ and κ as a parameter.

3. Theoretical considerations

3.1 Thermodynamics

To mimic a situation frequently encountered in sorption experiments, we treat the confined fluid as a semi-open system within the framework of phenomenological thermodynamics. This perception is motivated by the fact that, in parallel sorption experiments, the fluid confined to some mesoporous matrix is assumed to be in thermodynamic equilibrium with a (quasi-infinite) bulk reservoir with which it may exchange fluid matter and heat. Under these conditions and for a quantitative discussion of phase behaviour of the confined fluid, the semi-grand potential Ω turns out to be the relevant thermodynamic potential. Following the treatment of [3], the exact differential of Ω may be cast as

$$\mathrm{d}\Omega(T,\mu,N_{\mathrm{s}},\boldsymbol{\sigma}) = -\mathcal{S}\mathrm{d}T - N\mathrm{d}\mu + 2\mu_{\mathrm{s}}\mathrm{d}N_{\mathrm{s}} + V_0\mathrm{Tr}(\boldsymbol{\tau}\mathrm{d}\boldsymbol{\sigma}), \quad (3.1)$$

where T denotes temperature, $\mathcal{S}$ entropy, μ and μ_{s} are the chemical potentials of fluid molecules and substrate atoms, respectively, and $V_0 = s_{x0}s_{y0}s_{z0}$ is the volume of a finite rectangular lamella of the confined fluid in an (yet to be specified) unstrained reference state, where $s_{\alpha 0}$ is the side length of the lamella in the (Cartesian) α-direction; the remainder of the infinitely large confined fluid constitutes the surroundings of the lamella in the usual thermodynamic sense.

In Equation (3.1), the mechanical work contribution is expressed in terms of the trace Tr of a product of stress $\boldsymbol{\tau}$ and conjugate (infinitesimal) strain tensors $\mathrm{d}\boldsymbol{\sigma}$ [3]. As demonstrated in [3], these quantities can be represented by symmetric 3×3 matrices. Employing Cartesian coordinates and in the absence of shear strains, we have

$$\boldsymbol{\tau} = \frac{1}{2}\begin{pmatrix} 2\tau_{xx} & \tau_{\mathrm{xy}} & \tau_{\mathrm{xz}} \\ \tau_{\mathrm{xy}} & 2\tau_{yy} & \tau_{\mathrm{yz}} \\ \tau_{\mathrm{xz}} & \tau_{\mathrm{yz}} & 2\tau_{zz} \end{pmatrix} \quad (3.2a)$$

$$\boldsymbol{\sigma} = \begin{pmatrix} \sigma_{xx} & 0 & 0 \\ 0 & \sigma_{yy} & 0 \\ 0 & 0 & \sigma_{zz} \end{pmatrix} = \begin{pmatrix} \tilde{s}_x/s_{x0} - 1 & 0 & 0 \\ 0 & \tilde{s}_y/s_{y0} - 1 & 0 \\ 0 & 0 & \tilde{s}_z/s_{z0} - 1 \end{pmatrix}, \quad (3.2b)$$

where $\tilde{s}_\alpha$ denotes the side lengths of a rectangular lamella of the fluid in a strained state.

Equations (3.1) to (3.2b) apply to the system of interest, namely a slit pore with thermally corrugated walls as the most general case. These expressions become somewhat simpler for the reference system. Because, in this latter case, the walls lack any distinct atomic structure, the fluid is isotropic in the x–y plane perpendicular to the confining substrates. We may exploit this isotropy and define

$$\tau_{\parallel} \equiv \tau_{xx} = \tau_{yy} \quad (3.3a)$$

$$\frac{\sigma_{\parallel}}{2} \equiv \sigma_{xx} = \sigma_{yy}. \quad (3.3b)$$

Moreover, we may re-express V_0 as

$$V_0 = s_{x0}s_{y0}s_{z0} = A_0 s_{z0}, \quad (3.4)$$

where A_0 is the area of the z-directed face of the lamella in the unstrained reference state. Introducing $A = \sigma_{\parallel}A_0$ as the z-directed area of the lamella in a strained state, it is straightforward to verify from Equations (3.2)–(3.4) that

$$\mathrm{d}\Omega(T,\mu,N_{\mathrm{s}},A,s_z) = -\mathcal{S}\mathrm{d}T - N\mathrm{d}\mu + 2\mu_{\mathrm{s}}\mathrm{d}N_{\mathrm{s}} + \tau_{\parallel}s_{z0}\mathrm{d}A + \tau_{zz}A_0\mathrm{d}s_z. \quad (3.5)$$

Then, it is also clear that the confined fluid is homogeneous across each of the x–y planes stacked along the z-direction. Therefore, Ω in Equation (3.5) turns out to be a homogeneous function of degree 1 in its extensive (natural) variable A. We may therefore employ Euler's theorem (see Appendix A.3 of [3]) and introduce the semi-grand potential density of the reference system via

$$\omega^{\mathrm{ref}} \equiv \frac{\Omega^{\mathrm{ref}}}{As_{z0}} = \frac{\Omega^{\mathrm{ref}}}{V} = \tau_{\parallel}^{\mathrm{ref}}, \quad T,\mu,N_{\mathrm{s}},s_z = \mathrm{const.} \quad (3.6)$$

A similar expression is not obtained for the system of interest because the discrete (atomic) structure of the

substrates destroys homogeneity and isotropy of the confined fluid in the $x-y$ plane. However, regardless of the validity of Equation (3.6), the (exact) thermodynamic relations

$$\left(\frac{\partial\omega}{\partial\mu}\right)_{\{\cdot\}} = -\rho < 0 \tag{3.7a}$$

$$\left(\frac{\partial^2\omega}{\partial\mu^2}\right)_{\{\cdot\}} = -\rho^2\kappa_{\mathrm{T}} < 0 \tag{3.7b}$$

hold, where $\rho \equiv \langle N\rangle/V$ is the mean (number) density of the fluid, κ_{T} is its isothermal compressibility, and $\{\cdot\}$ is a shorthand notation to indicate that the differentiation is to be performed with T, N_{s} and $\boldsymbol{\sigma}$ being held fixed. Because of Equations (3.7a) and (3.7b), we conclude that curves $\omega(\mu)$ are monotonously decaying and concave.

Thus, under favourable thermodynamic conditions, one anticipates phase coexistence at intersections $\mu_x^{\alpha\beta}$ at which

$$\omega^{\alpha}(\mu_x^{\alpha\beta}) = \omega^{\beta}(\mu_x^{\alpha\beta}) \tag{3.8}$$

for a pair of phases α and β. Suppose $\rho^{\alpha} < \rho^{\beta}$, it follows that phase α is thermodynamically stable for $\mu < \mu_x^{\alpha\beta}$, whereas phase β is stable if the inequality $\mu > \mu_x^{\alpha\beta}$ holds.

3.2 Statistical thermodynamics

The connection with a microscopic level of description is established by statistical thermodynamics. To that end,

$$\Omega(T,\mu,N_{\mathrm{s}},\boldsymbol{\sigma}) = -k_{\mathrm{B}}T\ln\Xi(T,\mu,N_{\mathrm{s}},\boldsymbol{\sigma}) \tag{3.9}$$

is the key expression, where k_{B} is Boltzmann's constant, and

$$\Xi(T,\mu,N_{\mathrm{s}},\boldsymbol{\sigma}) = \sum_{N=0}^{\infty}\exp(\beta\mu N)\mathcal{Q}(T,N,N_{\mathrm{s}},\boldsymbol{\sigma}) \tag{3.10}$$

is the semi-grand canonical partition function, where $\beta \equiv 1/k_{\mathrm{B}}T$ [26].

In the classical limit, with which we are exclusively concerned in this work, the canonical ensemble partition function may be cast as

$$\mathcal{Q} = \frac{\mathcal{Z}}{\Lambda^{3(N+2N_{\mathrm{s}})}N!}, \tag{3.11}$$

where

$$\Lambda = \frac{h}{\sqrt{2\pi m k_{\mathrm{B}}T}} \tag{3.12}$$

is the thermal de Broglie wavelength. The specific form of Equation (3.11) results from an integration over momentum subspace formed by the N fluid molecules and $2N_{\mathrm{s}}$ substrate atoms, each of which possesses three translational degrees of freedom. Substrate atoms, which are bound to their equilibrium lattice sites (see Equation (2.8)), are distinguishable such that only the factor $1/N!$ arises for the (indistinguishable) fluid molecules in the denominator of Equation (3.11).

For our system of interest, the configuration integral in Equation (3.11) is given by

$$\mathcal{Z}(T,N,N_{\mathrm{s}},\boldsymbol{\sigma}) = \int \mathrm{d}\boldsymbol{R}\int \mathrm{d}\boldsymbol{R}_{\mathrm{s}}\exp[-\beta U(\boldsymbol{R},\boldsymbol{R}_{\mathrm{s}};\kappa)], \tag{3.13}$$

where the dependence on the (compressional) strains $\boldsymbol{\sigma}$ is buried in the limits of integration with respect to fluid–particle coordinates. The integration over substrate-atom configurations reflects the thermal coupling between the substrate and the confined fluid. In other words, for finite κ, the substrates cannot be treated as an external field but are part of the system in the same spirit in which the configuration of a disordered porous matrix enters the statistical–physical analysis of quenched–annealed models of complex mesoporous materials (see, for example, Chapter 7.2 of [3]). From Equations (2.9), (3.1) and (3.9)–(3.13), all microscopic expressions for thermo-mechanical properties of the system of interest can be derived [16].

However, in this work, we are concerned with the phase behaviour of the confined fluid. As we will explain shortly (see Section 3.3), this requires a computation of the stress $\tau_{\parallel}$ acting in directions perpendicular to the substrate normal in the reference system. According to Section 2.2, the substrates in the reference system are both structureless (see Equations (2.5) and (2.6)) and rigid. Because of these features we may replace $\mathcal{Z}(T,N,N_{\mathrm{s}},\boldsymbol{\sigma})$ by the simpler expression

$$\mathcal{Z}^{\mathrm{ref}}(T,N,A,s_z) = \int \mathrm{d}\boldsymbol{R}\exp[-\beta(U_{\mathrm{ff}} + U_{\mathrm{fs}}^{\mathrm{ref}})]. \tag{3.14}$$

In Equation (3.14), $U_{\mathrm{fs}}^{\mathrm{ref}}$ depends only on the z-coordinates of the fluid molecules. Thus, $U_{\mathrm{fs}}^{\mathrm{ref}}$ may be interpreted as the potential energy due to a static, inhomogeneous, external field acting on a configuration of fluid molecules in the z-direction. From Equations (3.5), (3.9), (3.11) and (3.14), it is then a simple matter to verify that

$$\begin{aligned}\tau_{\parallel}^{\mathrm{ref}} &= \frac{1}{s_{z0}}\left(\frac{\partial\Omega^{\mathrm{ref}}}{\partial A}\right)_{\{\cdot\}} = -\frac{k_{\mathrm{B}}T}{s_{z0}}\left(\frac{\partial\ln\Xi^{\mathrm{ref}}}{\partial A}\right)_{\{\cdot\}} \\ &= -\frac{\langle N\rangle k_{\mathrm{B}}T}{V} + \frac{1}{4V}\left\langle\sum_{i=1}^{N}\sum_{j=1\neq i}^{N}u'(r_{ij})r_{ij}\right. \\ &\quad\left.\times\left[(\hat{\boldsymbol{r}}_{ij}\cdot\hat{\boldsymbol{e}}_{\mathrm{x}})^2 + (\hat{\boldsymbol{r}}_{ij}\cdot\hat{\boldsymbol{e}}_{\mathrm{y}})^2\right]\right\rangle,\end{aligned} \tag{3.15}$$

where $\boldsymbol{r} = r\hat{\boldsymbol{r}}$ and $\hat{\boldsymbol{e}}_\alpha$ is a unit vector along the α-axis of the (Cartesian) coordinate system. In Equation (3.15), angular brackets denote ensemble averages in the grand canonical ensemble such that, together, Equations (3.6) and (3.15) provide a 'mechanical' molecular route to the grand potential density.

3.3 Perturbation theory

Unfortunately, such a 'mechanical' expression for ω does not exist for the system of interest (see Section 3.1 and [27]). To compute ω for our system of interest despite this deficiency in symmetry, we employ thermodynamic perturbation theory as suggested by Zwanzig [28] back in 1954 (see also [3,26]) and write

$$\begin{aligned} U(\lambda) &= U_{\mathrm{ff}} + (1-\lambda)U_{\mathrm{fs}}^{\mathrm{ref}} + \lambda(U_{\mathrm{fs}} + U_{\mathrm{ss}}) \\ &\equiv U_{\mathrm{ff}} + U_{\mathrm{fs}}^{\mathrm{ref}} + \lambda\Phi \end{aligned} \tag{3.16}$$

for the total configurational energy, where $\lambda \in [0,1]$ is a dimensionless parameter serving as a (continuous) 'switch' between the reference system ($\lambda = 0$) and the system of interest ($\lambda = 1$). The function Φ is introduced in Equation (3.16) merely for notational convenience.

Through Equations (3.9)–(3.11), (3.13) and (3.16), it is then evident that the (semi-) grand potential formally becomes a function of the coupling parameter λ. Thus, we may differentiate $\Omega(\lambda)$ with respect to the coupling parameter and obtain

$$\begin{aligned} \frac{\mathrm{d}\Omega(\lambda)}{\mathrm{d}\lambda} &= \frac{1}{\Xi(\lambda)} \sum_{N=0}^{\infty} \frac{\exp(\beta\mu N)}{\Lambda^{3(N+2N_{\mathrm{s}})} N!} \\ &\quad \times \int \mathrm{d}\boldsymbol{R} \int \mathrm{d}\boldsymbol{R}_{\mathrm{s}} \Phi(\boldsymbol{R}, \boldsymbol{R}_{\mathrm{s}}; \kappa) \exp[-\beta U(\lambda)] \\ &= \langle \Phi(\boldsymbol{R}, \boldsymbol{R}_{\mathrm{s}}; \kappa) \rangle_\lambda . \end{aligned} \tag{3.17}$$

In Equation (3.17), the angular brackets denote an average in the (semi-) grand canonical ensemble in which the distribution of microstates is governed by $U(\lambda)$ for a particular value of the coupling parameter λ. We may formally integrate this last expression, which gives

$$\begin{aligned} \omega(\lambda) &= \omega(0) + \frac{1}{V} \int_0^\lambda \mathrm{d}\lambda' \langle \Phi(\boldsymbol{R}, \boldsymbol{R}_{\mathrm{s}}; \kappa) \rangle_{\lambda'} \\ &= \tau_{\parallel}^{\mathrm{ref}} + \frac{1}{V} \int_0^\lambda \mathrm{d}\lambda' \langle \Phi(\boldsymbol{R}, \boldsymbol{R}_{\mathrm{s}}; \kappa) \rangle_{\lambda'} . \end{aligned} \tag{3.18}$$

The expression on the second line of Equation (3.18) follows because $\lambda = 0$ corresponds to the reference system (see Equation (3.16)), where Equation (3.6) holds.

4. Results

Henceforth, all quantities are expressed in suitable dimensionless (i.e. 'reduced') units. For example, energies are given in units of ε, temperature in units of $\varepsilon/k_{\mathrm{B}}$ and length in units of σ. Other quantities like stress, density or the binding parameter are expressed in terms of combinations of these 'basic' units such as ε/σ^3, σ^3 or ε/σ^2, respectively. Unless otherwise stated, all the simulations are carried out at a sufficiently subcritical temperature $T = 1.0$.

4.1 Phase behaviour and substrate 'softness'

Equation (3.18) permits numerical access to the grand potential density of the system of interest $\omega(\lambda = 1)$. Operationally speaking, we need to compute $\tau_{\parallel}^{\mathrm{ref}}$ via Equation (3.15) and $\langle \Phi(\boldsymbol{R}, \boldsymbol{R}_{\mathrm{s}}; \kappa) \rangle_\lambda$ in a sequence of (typically 10–20) individual Monte Carlo simulations for discrete values $0 \leq \lambda \leq 1$. The integral in Equation (3.18) is then evaluated numerically by means of a standard quadrature algorithm [29].

To illustrate this procedure, we plot in Figure 2 $\omega(\lambda)$ for $\kappa = 10^4$ and 30. A binding strength of $\kappa = 10^4$ is large enough to prevent substrate atoms from departing appreciably from their equilibrium lattice sites during the course of the simulation. In other words, $\kappa = 10^4$ corresponds to the limiting case of a perfectly rigid substrate for all practical purposes. This is because even vanishingly minute deviations of the actual position of any substrate atom from its equilibrium lattice site are associated with a substantial potential energy penalty (see Equation (2.8)).

As can be seen from respective plots in Figure 2(a,b), datasets coincide for $\lambda = 0$ corresponding to the reference system as they must. At the lower value $\kappa = 30$, the substrate may be deformed on account of the interaction with neighbouring substrate atoms, the coupling to the confined fluid and the thermal energy of each substrate atom. However, plots in Figure 2 show that regardless of κ, $\omega(\lambda)$ is a monotonically decreasing function of the coupling parameter, where the smaller the magnitude of the grand potential is, the more rigid the substrate is. The deviation between both datasets increases slightly with increasing λ.

The monotonicity of $\omega(\lambda)$ is an important prerequisite for the perturbational approach described in Section 3.3. A monotonic variation of ω with λ implies that the confined fluid does not undergo a first-order phase transition during the course of the transformation.

The perturbational procedure described in Section 3.3 and illustrated by plots in Figure 2 now permits us to compute $\omega(\mu)$ along an isotherm that is subcritical with respect to the critical point of the fluid in confinement. To this end, we need to choose two initial values of the

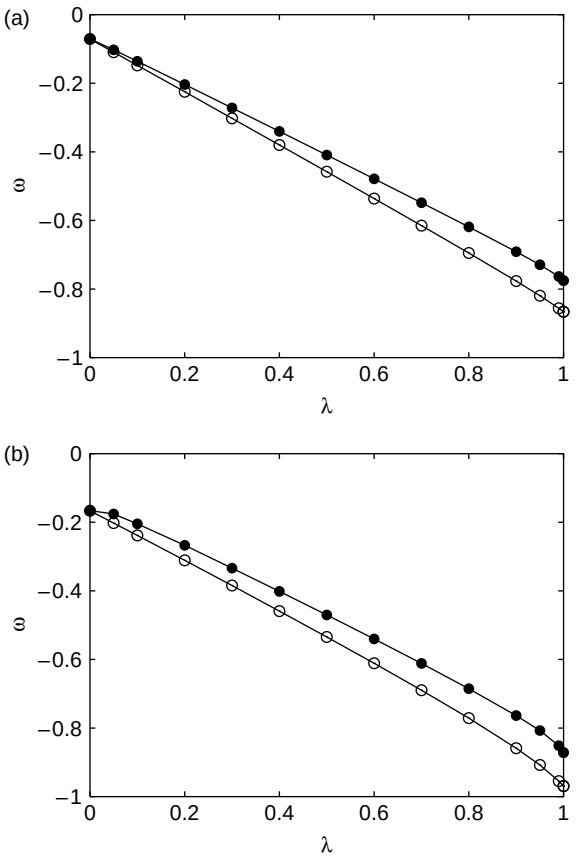

Figure 2. Plots of ω as a function of the coupling parameter λ (see Equation (3.18)) for $\kappa = 10^4$ (○) and $\kappa = 30$ (●). (a) Gas-like phases, $\mu = -11.6$ and (b) liquid-like phases, $\mu = -11.3$.

chemical potential μ_{in} corresponding to the one-phase region of the confined gas- and liquid-like phases. These values of the chemical potential are not known *a priori* so that some trial and error is required at this point.

We may then use μ_{in} in the reference system and compute $\omega(\mu_{\text{in}})$ in the system of interest via Equation (3.18). Once this value of the grand potential is known, we may use Equation (3.7a) in its integrated form

$$\omega(\mu) = \omega(\mu_{\text{in}}) - \int_{\mu_{\text{in}}}^{\mu} \mathrm{d}\mu' \rho(\mu'), \qquad T = \text{const} \qquad (4.1)$$

for different values of μ. The mean (number) density $\rho(\mu)$ appearing in the integrand in Equation (4.1) is computed as an ensemble average in semi-grand canonical ensemble Monte Carlo (SGCMC) simulations.

To analyse confinement effects and, in particular, the impact of substrate 'softness' on capillary condensation, it is necessary to determine first the location of the gas–liquid phase transition in the bulk. For a given subcritical temperature, this can be done in a straightforward fashion by computing the grand potential density in SGCMC simulations from

$$\omega = -P = -\frac{\langle N \rangle k_{\text{B}} T}{V} + \frac{1}{6V} \left\langle \sum_{i=1}^{N} \sum_{j=1 \neq i}^{N} u'(r_{ij}) r_{ij} \right\rangle. \quad (4.2)$$

This expression follows by noting that, in a homogeneous and isotropic bulk phase, the mechanical work term in Equation (3.1) can be simplified to $V_0 \mathrm{Tr}(\boldsymbol{\tau} \mathrm{d}\boldsymbol{\sigma}) = -P \mathrm{d}V$, where P is the (scalar) bulk pressure [3]. By manipulations similar to those leading to Equation (3.15), one may then derive the molecular expression for the bulk pressure on the far right-hand side of Equation (4.2) (see, for example, Appendix E.3.3 of [3]).

As expected, from the discussion in Section 3.1, a plot of $\omega(\mu)$ consists of two branches (Figure 3). According to Equation (3.7a), the one with the smaller (magnitude of the) slope (at smaller values of the chemical potential) along a subcritical isotherm $T = 1.0$ corresponds to gas, whereas the one with the larger (magnitude of the) slope pertains to liquid phases. Both branches intersect at the chemical potential of gas–liquid coexistence $\mu_x^{\text{gl}} \simeq -11.16$ (Figure 3(a)). At this point, the slope of $\omega(\mu)$ changes discontinuously because the densities of gas $\rho_x^{\text{g}} \simeq 0.059$ and liquid phases $\rho_x^{\text{l}} \simeq 0.634$ are different at coexistence (see Equation (3.7a)).

If one confines the fluid to a slit pore with a substrate separation $s_z = 6.8$, one expects a shift of gas–liquid phase coexistence to smaller bulk pressures because of the additional fluid–substrate attraction. Indeed, defining a reduced pressure P/P_0 (P_0 pressure of the saturated bulk gas at $\mu_x^{\text{gl}} \simeq -11.16$ and $T = 1.0$), the bulk phase transition occurs at $P/P_0 = 1$, which is outside the range of (reduced) pressures plotted in Figure 3(b). Therefore, the plot in Figure 3(b) reveals such a shift to a reduced pressure $P/P_0 \simeq 0.69$ as far as the (quasi-) rigid substrate at $\kappa = 10^4$ is concerned.

If one now couples the substrate thermally to the confined fluid by reducing the binding strength to $\kappa = 30$, the plots in Figure 3(b) show the enhanced deformability of the substrate that causes a shift of the coexistence pressure to a larger value $P/P_0 \simeq 0.72$. In other words, a slightly larger bulk pressure (or chemical potential μ) is required to initiate capillary condensation in the slit pore if the substrates respond to the phase change in the fluid material that they confine. Thus, a deformable substrate destabilises the confined liquid-like phases relative to the perfectly rigid substrate.

If the fluid is confined to a narrower slit pore of $s_z = 5.6$, capillary condensation occurs at a lower pressure $P/P_0 \simeq 0.61$ ($\kappa = 10^4$) and $P/P_0 \simeq 0.63$ ($\kappa = 30$) in accord with one's physical intuition (Figure 4(a)). A similar shift is observed if one maintains the pore width at $s_z = 6.8$ but reduces the temperature to $T = 0.8$ (Figure 4(b)). However, in both cases, it is noteworthy that

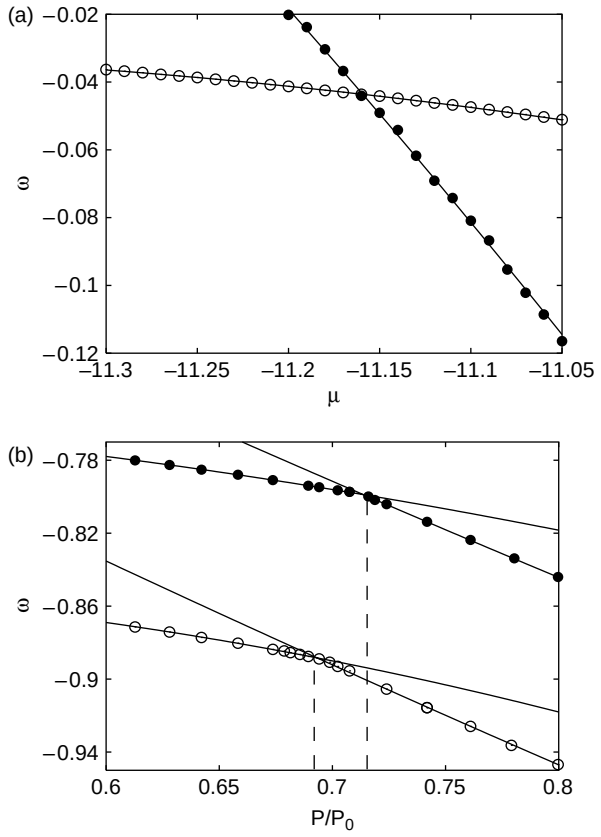

Figure 3. (a) The grand potential density ω as a function of μ in the bulk ($T = 1.0$). (b) As in (a) but for a fluid confined to a slit pore ($s_z = 6.8$) as a function of P/P_0 in a corresponding bulk system, where $P_0 = 0.043$ is determined from (a); $\kappa = 10^4$ (○) and $\kappa = 30$ (•). The vertical dashed line demarcates μ_x^{gl} (see text).

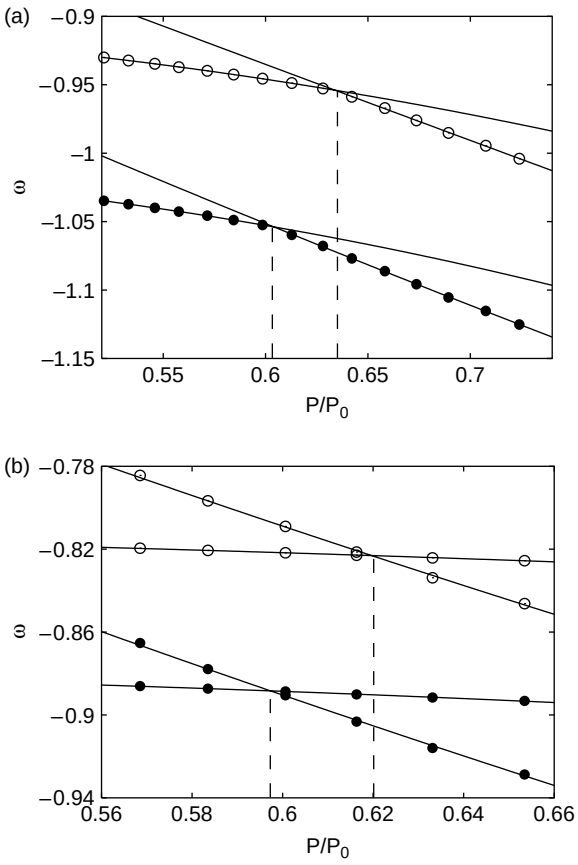

Figure 4. As in Figure 3(b) but for (a) $s_z = 5.6$, $T = 1.0$ and (b) $s_z = 6.8$, $T = 0.8$; $\kappa = 10^4$ (•), $\kappa = 30$ (○).

μ_x^{gl} is always larger for the deformable substrate compared with the (quasi-) rigid one.

4.2 Structural aspects

At this point, it seems worthwhile to address the associated structural changes in both the substrate and the confined fluid that occur on account of capillary condensation. We begin by considering the local density

$$\rho^{\mathrm{f,s}}(z) \equiv \frac{\langle N_{\mathrm{f,s}}(z)\rangle}{A_0 \delta s_z} \tag{4.3}$$

where the sub- and superscripts 'f' and 's' are used to refer to the local density of the confined fluid and the substrate atoms, respectively. Thus, $N_{\mathrm{f,s}}(z)$ is the respective number of fluid molecules or substrate atoms located in a parallelepiped of dimensions $s_{x0} \times s_{y0} \times \delta s_z$ centred on z, where we take $\delta s_z = 0.02$.

A typical plot of the local densities for the (quasi-) rigid ($\kappa = 10^4$) and a thermally coupled substrate ($\kappa = 30$) is presented in Figure 5 for the case $s_z = 6.8$. In the case of the (quasi-) rigid substrates,

$$\rho^{\mathrm{s}}(z) = \delta(z^{[1]} + s_z/2) + \delta(z^{[2]} - s_z/2), \tag{4.4}$$

where δ denotes the Dirac δ-function. As pointed out in Section 3.2 at $\kappa = 10^4$, the confining substrates may be perceived as an inhomogeneous, static external field imposed on the fluid molecules. As a consequence, the fluid appears to be stratified; that is, the centres of mass of fluid molecules arrange themselves preferentially in individual layers parallel with the substrate surfaces. Stratification of confined fluid phases is a well-known feature that has been noted many times in the previous literature for various systems and confinement scenarios such as hard spheres between hard surfaces [30,31], or soft spheres between atomically smooth [32] or structured substrates [33,34]. In addition, the substrates may be chemically patterned [15,35] or nonplanar [36–38]. Even in more complex fluids consisting of nonspherical molecules, stratification has been reported [39–42]. However, compared with fluids composed of spherically

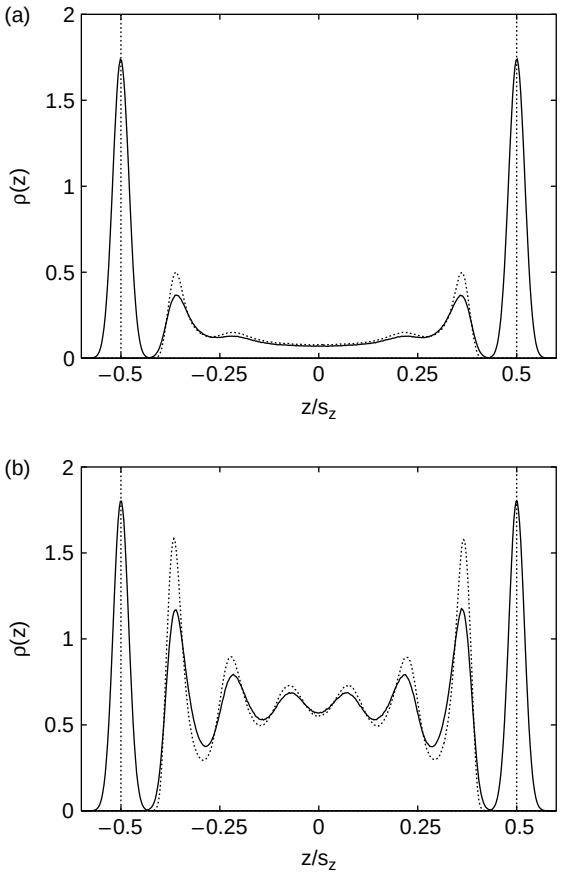

Figure 5. Plots of $\rho^{s}(z)$ and $\rho^{f}(z)$ as functions of position z/s_z ($s_z = 6.8$); quasi-rigid, atomically structured substrate, thermally coupled substrate at $\kappa = 10^4$ ($\cdots$) and $\kappa = 30$ (—). The portion of $\rho(z)$ centred on $|z|/s_z = 0.5$ refers to $\rho^{s}(z)$, whereas the remainder of the curves corresponds to $\rho^{f}(z)$; (a) $\mu = -11.6$ ($P/P_0 \simeq 0.58$) and (b) $\mu = -11.3$ ($P/P_0 \simeq 0.84$).

symmetric molecules, stratification appears to be diminished in the former cases on account of internal degrees of freedom.

In the present case, stratification diminishes as the substrate becomes increasingly deformable as one can see by comparing the plots of $\rho^{f}(z)$ for the (quasi-) rigid substrate ($\kappa = 10^4$) with the corresponding data for the 'softer' substrate at $\kappa = 30$ (Figure 5(a,b)). For this latter set of data, maxima are generally lower and minima less shallow than for $\kappa = 10^4$. The effects are more pronounced in Figure 5(b) than in Figure 5(a) on account of the higher density of liquid-like confined fluids compared with gas-like states. However, stratification, in general, diminishes as the distance from both walls becomes larger because of the decreasing importance of fluid–substrate interactions. This effect is also confirmed by the plots in Figure 5.

Moreover, an inspection of Figure 5 also shows that $\rho^{s}(z)$ for the thermally coupled substrate ($\kappa = 30$) cannot be represented by a δ-function but appears to be broadened because the substrate atoms possess thermal energy. For the time being, let us assume an ideal situation in which no fluid molecules are present between the substrates and we have switched off the coupling between neighbouring substrate atoms by setting $u(|\boldsymbol{r}_i^{[k]} - \boldsymbol{r}_j^{[k]}|) = 0$ (see Equation (2.8)). Because in this special case

$$U(\boldsymbol{R}_s) = \kappa \sum_{k=1}^{2} \sum_{i=1}^{N_s} \left| \boldsymbol{r}_i^{[k]} \pm \boldsymbol{r}_{i0}^{[k]} \right|^2 \tag{4.5}$$

the probability of finding *any* substrate atom at a position z is given by

$$\begin{aligned} P(z) &= \frac{1}{2}\sqrt{\frac{\kappa}{\pi k_B T}}\{\exp[-\beta\kappa(z - s_z/2)^2] \\ &\quad + \exp[-\beta\kappa(z + s_z/2)^2]\} \\ &\equiv P_-(z) + P_+(z)x, \end{aligned} \tag{4.6}$$

that is, a distribution consisting of two Gaussians centred at $z = \pm s_z/2$, provided that $\beta\kappa$ is sufficiently large. Note that in the limit $\kappa \to \infty$, Equation (4.6) is consistent with Equation (4.4) if we employ the definition of the Dirac δ-function via Gaussian distributions (see, for example, Appendix B.6.1 of Ref. [3]).

For the system of interest in which substrate atoms are coupled to one another and to a confined fluid of nonvanishing density, one anticipates deviations from this 'ideal' Gaussian form of the probability distributions. To quantify these deviations, we focus on the central moments of the distributions $P_{\pm}(z)$ defined via

$$\left\langle \left(z \pm \frac{s_z}{2} \right)^n \right\rangle \equiv \int_{-\infty}^{\infty} \mathrm{d}z \left(z \pm \frac{s_z}{2} \right)^n P_{\pm}(z), \tag{4.7}$$

where $P_{\pm}(z)$ is given by either $P_+(z)$ or $P_-(z)$ defined in Equation (4.6). Equation (4.7) is particularly useful for two reasons. First, for even n, one can verify by straightforward manipulations that

$$\mathsf{U} \equiv \frac{3\langle (z \pm s_z/2)^2 \rangle^2}{\langle (z \pm s_z/2)^4 \rangle} = 1, \tag{4.8}$$

if $P_{\pm}(z)$ are Gaussian. In turn, any deviation of the previous expression from the (ideal) value of 1 indicates a certain skewness of the probability distribution. Second, if the distribution possesses such a skewness, moments of odd order n do not necessarily vanish. In particular,

$$\langle z \rangle_{\pm} \equiv \int_{-\infty}^{\infty} \mathrm{d}z z P_{\pm}(z) \tag{4.9}$$

such that an *effective* slit-pore width may be defined via

$$s_z^{\text{eff}} \equiv \langle z \rangle_- - \langle z \rangle_+. \tag{4.10}$$

In the ideal case of Gaussian distributions $P_\pm(z)$, $s_z^{\text{eff}} = s_z$ because it is easy to verify from the previous expression that $\langle z \rangle_\pm = \mp s_z/2$. The plots in Figure 6 show that deviations from a Gaussian form of the density profile associated with the substrate atoms are minute but increase with decreasing 'stiffness' (i.e. increasing $1/\kappa$) with which substrate atoms are bound to their equilibrium lattice sites.

Let us now take the fluid confined between (quasi-) rigid walls ($\kappa = 10^4$) as the unstrained reference state in the sense of the thermodynamic analysis presented in Section 3.1, such that $s_{z0} = s_z$. This permits us to define the compressional strain σ_{zz} (see Equation (3.2b)) in the direction of the substrate normal as

$$\sigma_{zz} = \frac{s_z^{\text{eff}} - s_z}{s_z}. \tag{4.11}$$

An inspection of the plot of σ_{zz} in Figure 7 shows that the compressional strain increases at low pressures, indicating that for a confined gas-like phase the slit pore expands at first. Then, upon capillary condensation, it suddenly contracts but expands again as the pressure in the confined liquid-like phase is further raised. That the discontinuous change in σ_{zz} is, in fact, a signature of capillary condensation becomes evident upon comparison with the plot in Figure 3(b), which indicates that capillary condensation arises at $P/P_0 \simeq 0.72$. The sequence of initial expansion, sudden contraction at capillary condensation and subsequent expansion of the slit pore is characteristic and qualitatively independent of both pore width (Figure 8) and temperature over the range of P/P_0 studied. From the plots in Figure 8, one notes that the value of P/P_0 at capillary condensation increases with pore

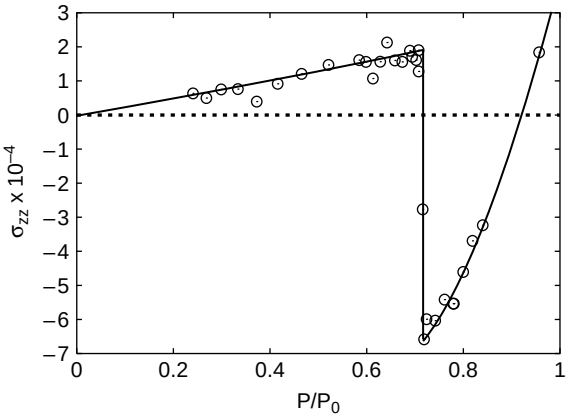

Figure 7. The compressional stress σ_{zz} as a function of reduced bulk pressure P/P_0 for a slit pore of width $s_z = 6.8$ and $T = 1.0$. $\kappa = 30$ (○), where the solid line is used to guide the eye, and $\kappa = 10^4$ (···).

width s_z as one would expect. Likewise, the magnitude of the discontinuous change in σ_{zz} at capillary condensation shrinks, which is again in accord with one's physical intuition. Thus, both the variation of σ_{zz} with P and that of P/P_0 at capillary condensation with κ are generic features associated with sorption strains. Moreover, the variation of σ_{zz} with P plotted in Figure 7 is consistent with the data obtained in recent SAXD experiments of nonpolar fluids confined to mesoporous silica [43].

However, qualitative changes in the compressional strain arise if one varies the strength of the fluid–substrate attraction as the plots in Figure 9 reveal. For example, for weak fluid–substrate interactions ($\zeta = 0.75$), the plot of σ_{zz} increases weakly up to $P/P_0 \simeq 0.9$, where capillary condensation sets in. The discontinuity in the sorption strain at capillary condensation is, on the other hand, more

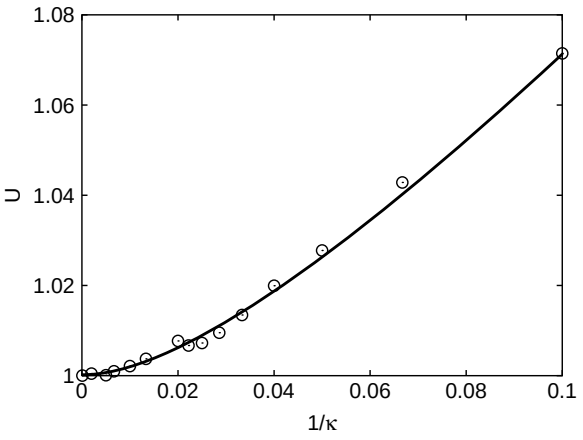

Figure 6. The skewness parameter U as a function of inverse binding strength $1/\kappa$.

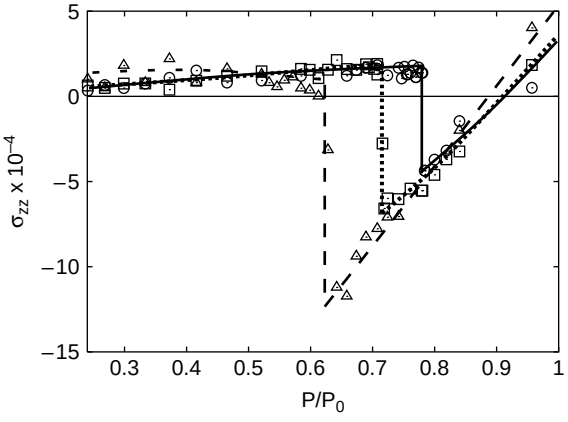

Figure 8. As in Figure 7, but for $s_z = 5.6$ (Δ), $s_z = 6.8$ (□) and $s_z = 8.0$ (○); $T = 1.0$ and $\kappa = 30$ for all datasets and lines are intended to guide the eye.

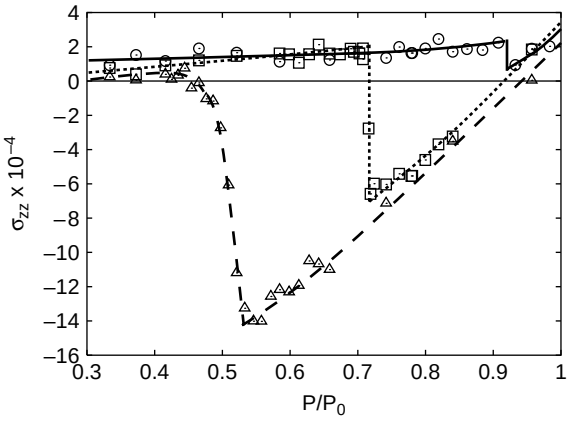

Figure 9. As in Figure 7, but $\zeta = 0.75$ (○), $\zeta = 1.0$ (□) and $\zeta = 1.5$ (Δ) (see Equation (2.7)); $T = 1.0$, $\kappa = 30$ and $s_z = 6.8$ for all datasets. Lines are intended to guide the eye.

pronounced for equally strong fluid–fluid and fluid–substrate interactions as clearly shown by the plot of σ_{zz} for $\zeta = 1.0$. Finally, if the fluid–substrate interaction exceeds that between a pair of fluid molecules (see the plot for $\zeta = 1.5$ in Figure 9), the discontinuous change in σ_{zz} is replaced by a more continuous variation of the sorption strain with pressure. However, comparing all three curves in Figure 9, one concludes that the sequence of (weak) initial increase (beyond the pressure range of multilayer adsorption), a more or less abrupt decrease when the pore fills with liquid and a subsequent increase of the sorption strain remains qualitatively unaffected provided the fluid–substrate interaction is sufficiently strong.

5. Summary and conclusions

In this study, we employ SGCMC simulations to study the structure and phase behaviour of a 'simple' fluid confined between two atomically structured solid substrates. The substrate atoms are coupled thermally to one another and to the fluid molecules. In addition, each substrate atom is bound to its equilibrium lattice site by a harmonic 'spring', where the binding parameter κ (i.e. the spring 'stiffness') controls the deformability (i.e. the 'rigidity') of the substrate. From a physical perspective, thermal coupling between the confined phases and the substrates causes the latter to 'respond' to whatever changes there may be in the thermodynamic state of the former (and vice versa). Therefore, the confining substrates can no longer be treated as a static, inhomogeneous, external field, an approach taken by the overwhelming number of theoretical works on confined fluids to date.

Thermal coupling of this sort complicates the statistical–physical treatment of such model systems. This is because the substrate atoms may depart from their equilibrium sites on account of their thermal energy and as a result of the interactions constituting the thermal coupling to the confined fluid phase. More specifically, the configuration integral involves an integration over substrate-atom configurations in excess of the standard integration over configurations of the fluid phase.

Our results indicate that for a sufficiently deformable substrate ($\kappa = 30$), the effective pore width s_z^{eff} changes as the confined fluid undergoes a discontinuous phase transition from gas- to liquid-like phases. The size change of the pore can be expressed quantitatively in terms of a compressional strain that changes discontinuously at capillary condensation. Under experimentally relevant conditions [43], the variation of the compressional strain with pressure turns out to be quite minute as far as the present subcritical thermodynamic states are concerned. Because the deformation of the substrate is in a sense determined by the magnitude of density fluctuations in the confined fluid (at a given rigidity of the substrate), we anticipate the effects reported here to be larger as one enters the near-critical regime of the confined phase. Work along these lines is currently under way [44]. The location of the phase transition is shifted to higher values of $P/P_0 < 1$ compared with a fluid confined between rigid solid substrates, indicating that the liquid phase is destabilised by pore deformation.

This shift can be rationalised as follows (O. Paris, private communication). Consider the limiting case $\kappa = 0$ in which substrate atoms are no longer bound to their equilibrium lattice sites. Because the LJ potential parameters $\{\varepsilon,\sigma\}$ are the same for fluid–fluid, fluid–substrate and substrate–substrate interactions, our system degenerates into a bulk system in the limit $\kappa = 0$. Thus, in this limit, one expects the condensation/evaporation of the fluid to occur at the bulk value $P/P_0 = 1$. On the other hand, for a rigid substrate as the other extreme case, capillary condensation occurs at $P/P_0 < 1$, where the shift of the phase transition relative to the bulk condensation is maximum. Hence, for finite but nonzero values of κ, one anticipates P/P_0 at capillary condensation to be somewhere in between the values characteristic of the rigid substrate and the corresponding bulk system in agreement with the plots in Figures 3 and 4.

In this context, it is important to realise that the case $\kappa = 30$ complies with a realistic situation because this binding strength is still large enough so that the substrates are solid-like in character. This conclusion is drawn on the basis of the Lindemann criterion, which assigns a specific value to the ratio δ_{L} between the average root-mean-square displacement of solid atoms and the average nearest-neighbour distance at the melting point of the solid. According to the work by Jin et al. [45] $\delta_{\mathrm{L}} \approx 0.12$–$0.13$ at the equilibrium melting temperature of a bulk crystal. Moreover, as was demonstrated by Zhengming et al. [46] in the one-phase region of a bulk crystal, the surface layer

of such a crystal exhibits less solid-like order than that characteristic of inner layers. Thus, one anticipates a larger Lindemann ratio for the surface layer of a three-dimensional crystal. In this work, we observe a value of $\delta_L \approx 0.16$ for the single-layer substrates, which is still smaller than $\delta_L \approx 0.2$ at which a bulk crystal becomes thermodynamically unstable [45]. Noting that the substrates consist only of a single layer of atoms and in view of [45,46], we conclude that our substrates remain solid-like under the chosen thermodynamic conditions.

Given that the conditions of this study seem sufficiently realistic, what is the significance of a thermal fluid–substrate coupling for parallel experiments? As we shall show in detail elsewhere [43], the strain measured for a nonpolar fluid adsorbed by mesoporous silica exhibits a pressure dependence in semi-quantitative agreement with the curve presented in Figure 7. Therefore, compared with the ideal case of rigid substrate surfaces, one expects a shift of the location of the experimental phase transition similar to the one shown in Figure 3(b). This shift, which should be of the order of a few per cent, is large enough to be accessible experimentally in principle. However, in experiments, the ideal case of rigid substrates can almost never be realised, which makes a direct comparison with the present theoretical results rather challenging.

Nevertheless, the present study demonstrates a synergistic effect; that is, the substrate responds to the thermodynamic state of the confined fluid, which, in turn, affects the fluid's phase behaviour. This synergistic effect is also expected to affect other types of phase transitions in nanoconfinement. For example, undercooled nanoconfined water does not freeze in the immediate vicinity of but only at larger distances from the pore walls, presumably on account of severe strains that prevent such vicinal water from forming solid-like structures [47]. These strains should be capable of deforming the pore walls similar to what is observed here. Another example is nanoconfined mesophases of anisometric molecules, where molecular packing and orientation should exert strains on the pore walls. Implications from sorption strains on the phase behaviour and vice versa might be expected particularly for fluids in very compliant nanoporous systems. A particular interesting case in this respect is the action of water in biological tissues, e.g. the movements of plants driven by changes in humidity [48].

Acknowledgements

This work was supported by the Deutsche Forschungsgemeinschaft within the framework of the Sonderforschungsbereich 448 'Mesoskopisch strukturierte Verbundsysteme'. Moreover, we are indebted to S.H.L. Klapp (Technische Universität Berlin) and O. Paris (Max-Planck-Institut für Kolloid- und Grenzflächenforschung) for their valuable discussions.

Note

1. Email: gerrit.guenther@fluids.tu-berlin.de

References

[1] R. Evans and A.O. Parry, *Liquids at interfaces: what can a theorist contribute?*, J. Phys. Condens. Matter 2 (1990), SA15.
[2] L.D. Gelb, K.E. Gubbins, R. Radhakrishnan, and M. Sliwinska-Bartkowiak, *Phase separation in confined systems*, Rep. Prog. Phys. 62 (1999), pp. 1573–1659.
[3] M. Schoen and S.H.L. Klapp, *Nanoconfined Fluids. Soft Matter between Two and Three Dimensions*, Wiley-VCH, Hoboken, 2007.
[4] W. Thomson (the later Lord Kelvin), *On the equilibrium of a vapour at a curved surface of liquid*, Phil. Mag. 7 (1870), pp. 448–452.
[5] G.V. Burgess, D.H. Everett, and S. Nuttal, *Adsorption hysteresis in porous materials*, Pure Appl. Chem. 61 (1989), pp. 1845–1852.
[6] A.P.Y. Wong and M.H.W. Chan, *Liquid–vapor critical point of ^{4}He in aerogel*, Phys. Rev. Lett. 65 (1990), pp. 2567–2570.
[7] A. de Keizer, T. Michalski, and G.H. Findenegg, *Fluids in pores: experimental and computer simulation studies of multilayer adsorption, pore condensation and critical-point shifts*, Pure Appl. Chem. 63 (1991), pp. 1495–1502.
[8] A.P.Y. Wong, S.B. Kim, W.I. Goldburg, and M.H.W. Chan, *Phase separation, density fluctuation, and critical dynamics of N_2 in aerogel*, Phys. Rev. Lett. 70 (1993), pp. 954–957.
[9] W.D. Machin, *Temperature dependence of hysteresis and the pore size distributions of two mesoporous adsorbents*, Langmuir 10 (1994), pp. 1235–1240.
[10] M. Thommes and G.H. Findenegg, *Pore condensation and critical-point shift of a fluid in controlled-pore glass*, Langmuir 10 (1994), pp. 4270–4277.
[11] D. Zhao, J. Feng, Q. Huo, N. Melosh, G.H. Frederickson, B.F. Chmelka, and G.D. Stucky, *Triblock copolymer syntheses of mesoporous silica with periodic 50 to 300 angstrom pores*, Science 279 (1998), pp. 548–552.
[12] D. Zhao, Q. Huo, J. Feng, B.F. Chmelka, and G.D. Stucky, *Nonionic triblock and star diblock copolymer and oligomeric surfactant syntheses of highly ordered, hydrothermally stable, mesoporous silica structures*, J. Am. Chem. Soc. 120 (1998), pp. 6024–6036.
[13] T. Hoffmann, D. Wallacher, P. Huber, R. Birringer, K. Knorr, A. Schreiber, and G.H. Findenegg, *Small-angle x-ray diffraction of Kr in mesoporous silica: effects of microporosity and surface roughness*, Phys. Rev. B 72 (2005), 064122.
[14] K. Binder, J. Horbach, A. Milchev, M. Müller, and R. Vink, *Monte Carlo Simulations of phase transitions of systems in nanoscopic confinement*, Comput. Phys. Commun. 177 (2007), pp. 140–145.
[15] M. Schoen, *Fluid bridges confined between chemically nanopatterned solid substrates*, Phys. Chem. Chem. Phys. 10 (2008), pp. 223–256.
[16] D.J. Diestler and M. Schoen, *Fluids in micropores. V. Effects of thermal motion in the walls of a slit-micropore*, J. Chem. Phys. 104 (1996), pp. 6784–6795.
[17] H. Namatsu, K. Kurihara, M. Nagase, K. Iwadate, and K. Murase, *Dimensional limitations of silicon nanolines resulting from pattern distortion due to surface tension of rinse water*, Appl. Phys. Lett. 66 (1995), pp. 2655–2657.
[18] P. Kowalczyk, A. Ciach, and A.V. Neimark, *Adsorption-induced deformation of microporous carbons: pore size distribution effect*, Langmuir 24 (2008), pp. 6603–6608.
[19] E.A. Ustinov and D.D. Do, *Effect of adsorption deformation on thermodynamic characteristics of a fluid in slit pores at sub-critical conditions*, Carbon 44 (2006), pp. 2652–2663.
[20] G.A. Zickler, S. Jähnert, W. Wagermeier, S.S. Funari, G.H. Findenegg, and O. Paris, *Physisorbed films in periodic mesoporous silica studied by* in situ *synchrotron small-angle diffraction*, Phys. Rev. B 73 (2006), p. 184109.
[21] G.W. Scherer, *Dilatation of porous glass*, J. Am. Ceram. Soc. 69 (1986), pp. 473–480.
[22] G. Dolino, D. Bellet, and C. Faivre, *Adsorption strains in porous silicon*, Phys. Rev. B 54 (1996), pp. 17919–17929.

[23] T. Herman, J. Day, and J. Beamish, *Deformation of silica aerogel during fluid adsorption*, Phys. Rev. B 73 (2006), 094127.
[24] K. Binder and P. Fratzl, in *Materials Science and Technology*, Vol. 5, G. Kostorz ed., Wiley-VCH, Weinheim, 2001, pp. 409–490.
[25] N.B. Wilding and M. Schoen, *Absence of simulation evidence for critical depletion in slit pores*, Phys. Rev. E 60 (1999), pp. 1081–1083.
[26] J.P. Hansen and I.R. McDonald, *Theory of Simple Liquids*, Academic Press, London, 1986.
[27] M. Schoen, *On the uniqueness of stratification-induced structural phase transitions in confined films*, Ber. Bunsenges. Phys. Chem. 100 (1996), p. 8.
[28] R. Zwanzig, *High-temperature equation of state by a perturbation method. I. Nonpolar gases*, J. Chem. Phys. 22 (1954), pp. 1420–1426.
[29] W.H. Press, B.P. Flannery, S.A. Teukolsky, and W.T. Vetterling, *Numerical recipes. The art of scientific computing (FORTRAN version)*, 1996. Chapter 4.
[30] J.E. Lane and T.H. Spurling, *Grand ensemble Monte Carlo calculation of the thermodynamic properties of a solid/vapour interface*, Aust. J. Chem. 29 (1976), pp. 2103–2121.
[31] J. Mittal, J.R. Errington, and T.M. Truskett, *Does confining the hard-sphere fluid between hard walls change its average properties?*, J. Chem. Phys. 126 (2007), 244708.
[32] I. Snook and W. van Megen, *Structure of dense liquids at solid interfaces*, J. Chem. Phys. 70 (1979), pp. 3099–3105.
[33] M. Schoen, J.H. Cushman, and D.J. Diestler, *Fluids in micropores. II. Self-diffusion in a simple classical fluid in a slit pore*, J. Chem. Phys. 88 (1988), pp. 1394–1404.
[34] D.P. Cao, X.R. Zhang, Z.G. Shen, J.F. Chen, and J. Yun, *Density functional theory of adsorption and phase behavior of the Lennard-Jones fluids confined in MCM-41 with a finite thickness*, Colloids. Surf. A Physicochem. Eng. Aspects 247 (2004), pp. 91–98.
[35] A. Valencia and R. Lipowsky, *Nucleation through a double barrier on a chemically patterned substrate*, Langmuir 20 (2004), pp. 1986–1996.
[36] M. Schoen and S. Dietrich, *Structure of a hard-sphere fluid in hard wedges*, Phys. Rev. E 56 (1997), pp. 499–510.
[37] A.O. Parry, C. Rascón, N.B. Wilding, and R. Evans, *Condensation in a Capped Capillary is a Continuous Critical Phenomenon*, Phys. Rev. Lett. 98 (2007), 226101.
[38] H. Bohlen, A.O. Parry, E. Díaz-Herrera, and M. Schoen, *Intrusion of fluids into nanogrooves – How geometry determines the shape of the gas-liquid interface*, Eur. Phys. J. E 25 (2008), pp. 103–115.
[39] A. Huerta, O. Pizio, and S. Sokolowski, *Phase transitions in an associating, network-forming, Lennard-Jones fluid in slit-like pores. II. Extension of the density functional method*, J. Chem. Phys. 112 (2000), pp. 4286–4295.
[40] S.T. Cui, P.T. Cummings, and H.D. Cochran, *Structural transition and solid-like behavior of alkane films confined in nano-spacing*, Fluid Phase Equilib. 183 (2001), pp. 381–387.
[41] T.M. Truskett, P.G. Debenedetti, and S. Torquato, *Thermodynamic implications of confinement for a waterlike fluid*, J. Chem. Phys. 114 (2001), pp. 2401–2418.
[42] A. Richter and T. Gruhn, *Structure formation and fractionation in systems of polydisperse attractive rods*, J. Chem. Phys. 125 (2006), 064908.
[43] G. Günther, J. Prass, O. Paris, and M. Schoen, *Novel insights into nanopore deformation caused by capillary condensation*, Phys. Rev. Lett. 101 (2008), 086104.
[44] G. Günther and M. Schoen, in preparation.
[45] Z.H. Jin, P. Gumbsch, K. Lu, and E. Ma, *Melting Mechanisms at the Limit of Superheating*, Phys. Rev. Lett. 87 (2001), p. 055703.
[46] J. Zhengming, Y. Genqing, C. Zhaonian, L. Xianghuai, and Z. Shichang, *The two-dimensional pair correlation function for the Si(001) surface: computer simulation results*, J. Phys. Condens Matter 6 (1994), pp. 1083–1088.
[47] A. Schreiber, I. Ketelsen, and G.H. Findenegg, *Melting and freezing of water in ordered mesoporous silica materials*, Phys. Chem. Chem. Phys. 3 (2001), pp. 1185–1195.
[48] R. Elbaum, L. Zaltzman, I. Burgert, and P. Fratzl, *The role of wheat awns in the seed dispersal unit*, Science 316 (2007), pp. 884–886.